Molecular Precision Engineering for Efficient Binary Organic Photovoltaics through Energy Level and Fibrillar Structure Modulation

Rui Zeng, Shengjie Xu,* Jiawei Deng, Senke Tan, Guanqing Zhou, Ming Zhang,* Lei Zhu, Fei Han, Xiaonan Xue,* Anyang Zhang, Hongtao Tan, Lingjie Zhang, Chenhui Zhu, Cheng Wang, Xuefei Wu, Zachary Fink, Thomas P. Russell, Yongming Zhang,
and Feng Liu*

Adjusting the energy levels and fibrillar morphology is paramount to enhancing the power conversion efficiency (PCE) of organic solar cells (OSCs). In the present study, an increase in the open-circuit voltage (V_{OC}) is facilitated through the elongation of the alkyl chain within AQx (namely AQx-8), aiming to decrease the free volume ratio (FVR). This reduction in FVR attenuates electron-phonon coupling, thereby augmenting emission efficiency and diminishing the non-radiative energy loss (ΔE_{nr}).
To further refine the energy levels and morphological characteristics, the external undecyl chain of AQx-8 is substituted with a shorter carbon chain and cyclohexane noted for its considerable steric hindrance (AQx-H). This alteration significantly mitigates intermolecular aggregation, expands the bandgap, and elevates the lowest unoccupied molecular orbital (LUMO) energy level, culminating in an elevated V_{OC} of 0.923 V in devices based on AQx-H. Morphological analysis reveals that blends based on AQx-H exhibit an

1

Organic solar cells (OSCs) have gained widespread attention as a promising renewable energy technology, attributed to their inherent advantages of flexibility, semi-transparency, low cost, and large-area printability, etc.[1–5] In particular, the development of active layer materials in the past few decades has led to a dramatic improvement in power conversion efficiency (PCE),[6–10] resulting in increased confidence in commercial applications. The rapid breakthrough in PCE in recent years is mainly attributed to the development of non-fullerene electron acceptors (NFAs) with highly tunable chemical structures, optoelectronic properties, and molecular stacking.[7,9,11–15] Among these, the Y-series molecules, adopting an A-DA'D-A configuration, stand out as the most efficacious, having achieved a PCE exceeding 19% in single-junction devices.[16–29]

R. Zeng, S. Xu, J. Deng, S. Tan, G. Zhou, M. Zhang, L. Zhu, F. Han,
A. Zhang, Y. Zhang, F. Liu
School of Chemistry and Chemical Engineering Frontiers Science Center for Transformative Molecules In situ Center for Physical Science
Center of Hydrogen Science Shanghai Jiao Tong University Shanghai 200240, P. R. China
E-mail: xushengjie@sjtu.edu.cn; i.m.zhangm@sjtu.edu.cn; fengliu82@sjtu.edu.cn

X. Xue
Shanghai OPV Solar New Energy Technology Co., Ltd. Shanghai 201210, P. R. China
E-mail: xuexiaonan@opvsolar.com

H. Tan
Power Research Institute of State Grid Shaanxi Electric Power Co., Ltd Xi'an 710199, P. R. China

L. Zhang
Meishan Duoneng Electric Power Construction Co., Ltd. Meishan 620000, P. R. China

C. Zhu, C. Wang
Advanced Light Source
Lawrence Berkeley National Laboratory Berkeley, CA 94720, USA

X. Wu, Z. Fink, T. P. Russell
Materials Sciences Division
Lawrence Berkeley National Laboratory Berkeley, CA 94720, USA

Z. Fink, T. P. Russell
Polymer Science and Engineering Department University of Massachusetts
Amherst, MA 01003, USA

Open-circuit voltage (V_{OC}), short-circuit current density (J_{SC}), and fill factor (FF) are the three key photovoltaic parameters that determine PCE. However, the deep-lying lowest unoccupied molecular orbital (LUMO) energy levels of Y-series NFAs engenders a comparatively diminished V_{OC}, thereby imposing constraints on further enhancements in PCE.[9] Meanwhile, the specificity of the structure and conformation of the Y-series NFAs led to the lack of viable sites for derivatization, complicating efforts to modulate the LUMO energy level via alterations to the conjugated backbone. Therefore, the focus of scholarly inquiry has increasingly shifted toward the modulation of alkyl chains as a primary avenue of research. Examples of Y-series NFAs alkyl side chain engineering begins with the modification of the inner chain 2-ethylhexyl. Hou et al. synthesized BTP-4F-12 by extending the alkyl chain length to 2-butyloctyl, and the improved crystallinity and electron mobility led to an increase in PCE to 16.5%, with a slight increase in V_{OC}.[30] Zou et al. synthesized N3 by changed the position of the branched chain from the 2nd to the 3rd position, and the optimal solubility and electronic properties led to an increased PCE of 15.98%, with a slight decrease in V_{OC}.[31] Empirical evidence has substantiated the challenge inherent in achieving a substantial elevation of the V_{OC} by modulating the LUMO energy level through the inner alkyl chain. Consequently, researchers have redirected their investigative focus toward the outer alkyl chain located at the β-position of the thienothiophene units. Yang et al. synthesized BTP-PhC6 by replacing the undecyl linear chain with 4-hexylphenyl, where the increased steric hindrance between the INCN-2F end-groups and PhC6 resulted in an upshifted of the LUMO energy, successfully boosting the V_{OC}.[32] In a further illustration of the efficacious implementation of steric hindrance, Sun et al. Introduced branched outer alkyl chains to synthesize L8-BO. This modification resulted in an elevation of the LUMO energy level by 0.17 eV compared to Y6, achieving a binary PCE of >18%, and an increase in V_{OC} to 0.87 V. These findings clearly indicate that the increase of steric hindrance at the external substitution site constitutes a potent strategy for achieving heightened V_{OC}.[22]

Our research endeavors have been directed toward the advancement of NFAs with high V_{OC}, and with the consideration of inducing a better-defined bicontinous morphology. The AQx-type acceptors featuring a quinoidal-enhancing quinoxaline moiety were developed, which show good potential to boost V_{OC} in the form of reduced energy loss due to its low recombination energy.[33,34] Unlike the 3D stacked observed in Y6, the theoretical and experimental results reveal that the prolonged inner alkyl chain within the 2D stacked form of AQx contributes to a reduced free volume ratio (FVR). It is beneficial to enhance emission efficiency and reduce ΔE_{nr}, realizing the improvement of V_{OC}.[35,36] However, the increased inner alkyl chain length induces improved miscibility between AQx and the polymer donor, leading less efficient phase separation that limits charge transport. Besides, in order to further enhance V_{OC}, the introduction of steric hindrance groups (e.g., 2-butyl octane) to the outer side substitution site may further intensify these effects. Accordingly, it becomes imperative to integrate new substituents at the outer β-site of the thienothiophene unit that reconcile the need for electronic property and morphology. In this work, we have synthesized the acceptor material AQx-H by introducing the ring-type cyclohexane side chain instead of linear side chain to the outer β-site, of using its physical chemistry property differences with the linear side chain in donor polymer to reduce inter-mixing and redirect molecular packing, thereby satisfying both aforementioned criteria. It is also revealed that D18:AQx-H blends display a better multi-length-scale fibril-like morphology, with better defined crystalline feature. Thus, the AQx-H-based device has achieved an impressive V_{OC} of 0.923 V based on the AQx backbone, resulting in one of the best performance (19.5%) with an appropriate J_{SC} of 26.40 mA cm^{-2} and FF of 79.87%. This efficiency has been certified as 19% by the National Photovoltaic Industry Metrology and Testing Center (NPVM).

2. Results

Figure 1a delineates the chemical structures of AQx-8 and AQx-H. Following the synthetic route in Figure 1b and Scheme S1 (Supporting Information), we successfully obtained the key intermediate cyclohexane-substituted TT-H, which subsequently facilitated the synthesis of AQx-H. Density functional theory (DFT) calculations were performed on acceptors to simulate the molecular geometry.[37] The calculation results are displayed in **Figure 2**a–d. For AQx-8, the dihedral angle between its central unit and the INCN-2F group is 0.14°. The integration of a cyclohexane ring, a unit characterized by significant steric hindrance, resulted in a slight increment in the dihedral angles for AQx-H, specifically to 0.34° and 0.89°. However, this modification does not appreciably affect the planarity of the molecule's backbone. Moreover, the electronic static potential (ESP) results of both acceptors reveal that they possess symmetrical and analogous electrostatic potentials, suggesting that alterations in the side chain exert an insubstantial impact on the overall electron cloud distribution within the molecule.

Figure 2e and Figure S1 (Supporting Information) depict the absorption characteristics of the pristine film and the blend film, respectively. The absorption spectrum of AQx-H demonstrates a pronounced blueshift in comparison to that of AQx-8 (the undecyl side chain substituted analog), which is attributed to the high steric hindrance of cyclohexane substitution. In the case of the blend films, AQx-H is characterized by an augmented molar absorption coefficient, thereby promoting more efficient light absorption. Figure 2f illustrates the energy levels of AQx-8 and AQx-H. The LUMO and the highest occupied molecular orbital (HOMO) energy levels were deduced by cyclic voltammetry, with the corresponding data presented in Figure S2 (Supporting Information). Accordingly, the LUMO/HOMO levels are −3.85/−5.60 eV for AQx-8 and −3.82/−5.65 eV for AQx-H. Notably, AQx-H exhibits elevated LUMO energy level, which is conducive to the enhancement of V_{OC}.

Figure 3a shows the device structure of ITO/ hole transport layer (HTL)/ Active Layer/ electron transport layer (ETL)/ Ag. The

Y. Zhang, F. Liu
State Key Laboratory of Fluorinated Functional Membrane Materials and Dongyue Future Hydrogen Energy Materials Company
Zibo, Shandong 256401, P. R. China
F. Liu
Suzhou Laboratory
Suzhou 215100, P. R. China

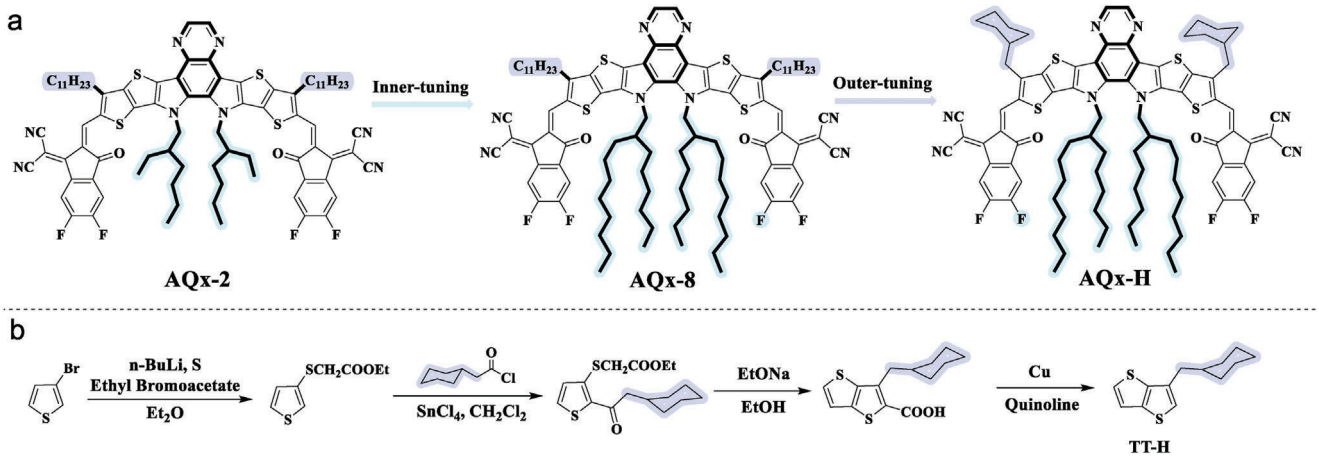

Figure 1. a) Chemical structures of AQx-2, AQx-8, and AQx-H acceptors. b) Synthetic route to the key intermediate TT-H.

blend films of D18:AQx-8 or D18:AQx-H were used as the active layer. The *J*–*V* characteristics and solar cell performances for the blends are shown in Figure 3b and summarized **Table 1**. The device optimization process is shown in Figure S3 and Table S1 (Supporting Information). The D18:AQx-8 device showed a maximum PCE of 17.8% with a V_{OC} of 0.894 V, a J_{SC} of 26.54 mA cm^{-2}, and an FF of 75.04%. For D18:AQx-H device, a much higher ef- ficiency of 19.5% was obtained with a V_{OC} of 0.923 V, a J_{SC} of
26.40 mA cm^{-2}, and an FF of 79.87%, which is among the highest efficiencies in binary OPV devices reported so far. The optimum device achieved a third-party certified PCE of 19.0% (documented in Figure S4, Supporting Information, by the NPVM, and certified result is shown in Figure 3c and Table 1. As shown in Figure S5a (Supporting Information), the external quantum efficiency (EQE) from relative spectral responsivity (SR) is calculated by following formula of

$$EQE\ (\square) = 100 \times \frac{1240 \times SR\ (\square)}{\square}\ (\%) \quad (1)$$

The relative SR curve given in certification report is normalized (from 0% to 100%), so the calculated result is not the absolute value. Compared with the EQE obtained in experiment as shown in Figure S5b (Supporting Information), the EQE obtained in experiment is generally consistent with the certification results. The higher V_{OC}, J_{SC} and FF indicate that both carrier

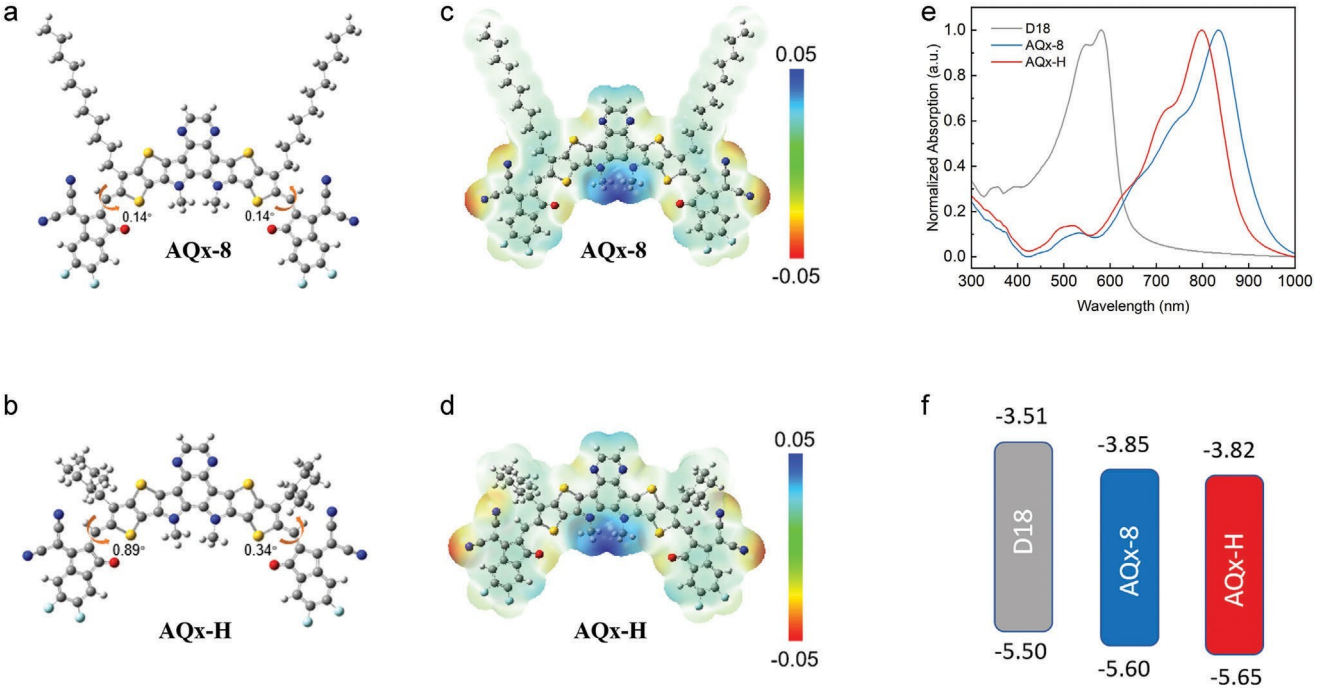

Figure 2. a) DFT calculation for geometry optimization of AQx-8 b) DFT calculation for geometry optimization of AQx-H. c) ESP of AQx-8. d) ESP of AQx-H. e) Normalized absorption of D18, AQx-8, and AQx-H. f) Energy level diagram of D18, AQx-8, and AQx-H.

Figure 3. a) device structure of ITO/HTL/BHJ/ETL/Ag. b) *J*–*V* curves and detailed parameters in different condition under

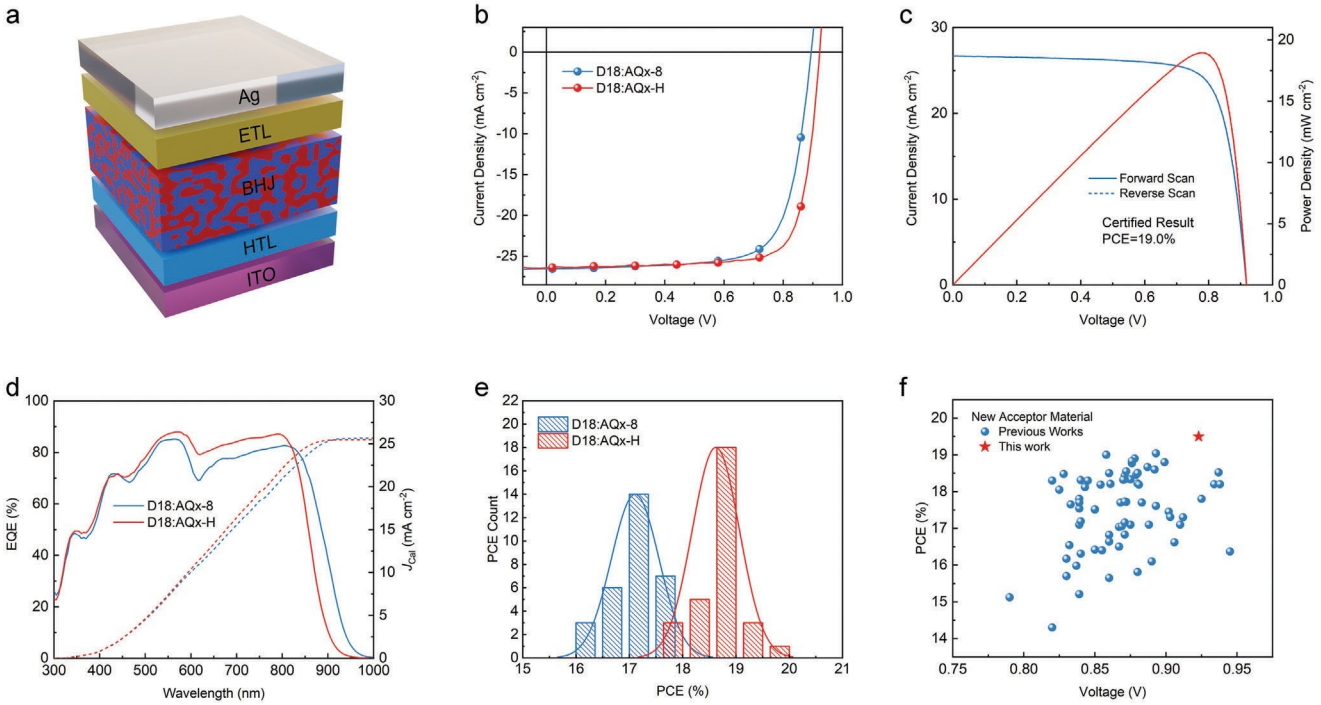

AM 1.5G, 100 mA cm^{-2}. c) EQE spectra and integrated J_{SC} in corresponding condition. d) The certified efficiency performance by the NPVM, China. e) Histogram of PCE measurement for devices in corresponding condition under AM 1.5G, 100 mA cm^{-2}. f) Plots of the PCE versus V_{OC} for the efficient new acceptors material reported in the literature.

generation and carrier transport are optimized, suggesting that a more favorable synergy of molecular design and morphology optimization is obtained. The EQEs and differences are presented in Figure 3d and Figure S6 (Supporting Information). Notably, the D18:AQx-H blend exhibits a more robust response across an extensive wavelength range, spanning from 450 to 800 nm. This enhanced response is attributed to the improved exciton dissociation and carrier collection efficiencies, which provide an optimal J_{SC} for D18:AQx-H device despite the blueshift in the absorption spectrum. The statistical distribution of the PCE across various device fabrication conditions is succinctly summarized in Figure 3e, which evidences the commendable reproducibil- ity of the device performance and high reliability of the process- ing strategy. An explicit comparison to the state-of-the-art new acceptor performance is given in Figure 3f. This analysis incorporates the present findings alongside 74 data points extracted from the extant literature, collectively indicating a substantial enhancement in the performance of the new acceptor materials.

The morphological characteristics of thin films composed of D18:AQx-8 and D18:AQx-H were meticulously examined, using grazing incidence wide-angle X-ray scattering (GIWAXS) to elucidate the crystalline structure of the materials.[38] As depicted in Figure S7 (Supporting Information), the pristine D18 film exhibits a predominantly face-on orientation, characterized by a lamellar peak at 0.30 Å^{-1} in the in-plane (IP) direction and a □-□ stacking peak at 1.70 Å^{-1}, primarily in the out-of-plane (OOP) direction. In the case of AQx-8, two distinct peaks are observable at 0.28 and 0.38 Å^{-1}, respectively, in the IP direction, accompanied by a □-□ stacking peak at 1.76 Å^{-1} in the OOP direction. As for AQx-H, a broad lamellar peak is seen at 0.38 Å^{-1} in the IP direction with a □-□ stacking peak at 1.76 Å^{-1} in the OOP direction. The crystallinity of AQx-H is notably less marked due to increased steric hindrance. This phenomenon is manifested by diminished ordering in both the lamellar and □–□ stacking directions. In the blended films, the 2D GIWAXS results are presented in **Figure 4**a,b, with 1D line profiles delineated along the OOP

Table 1. The efficiency for D18:AQx-8 and D18:AQx-H (certified) BHJ under AM 1.5G, 100 mA cm^{-2}. The average values are obtained from 30 individual experimental results.

BHJ	J_{SC} [mA cm^{-2}]	J_{Cal} [mA cm^{-2}]	V_{OC} [V]	FF [%]	PCE [%]
D18:AQx-8	26.54 (26.24 ± 0.32)	25.66	0.894 (0.895 ± 0.002)	75.04 (72.91 ± 2.54)	17.8 (17.1 ± 0.45)
D18:AQx-H	26.40 (26.05 ± 0.36)	25.48	0.923 (0.924 ± 0.002)	79.87 (77.48 ± 2.33)	19.5 (18.6 ± 0.44)
Certified	26.67		0.920	77.38	19.0

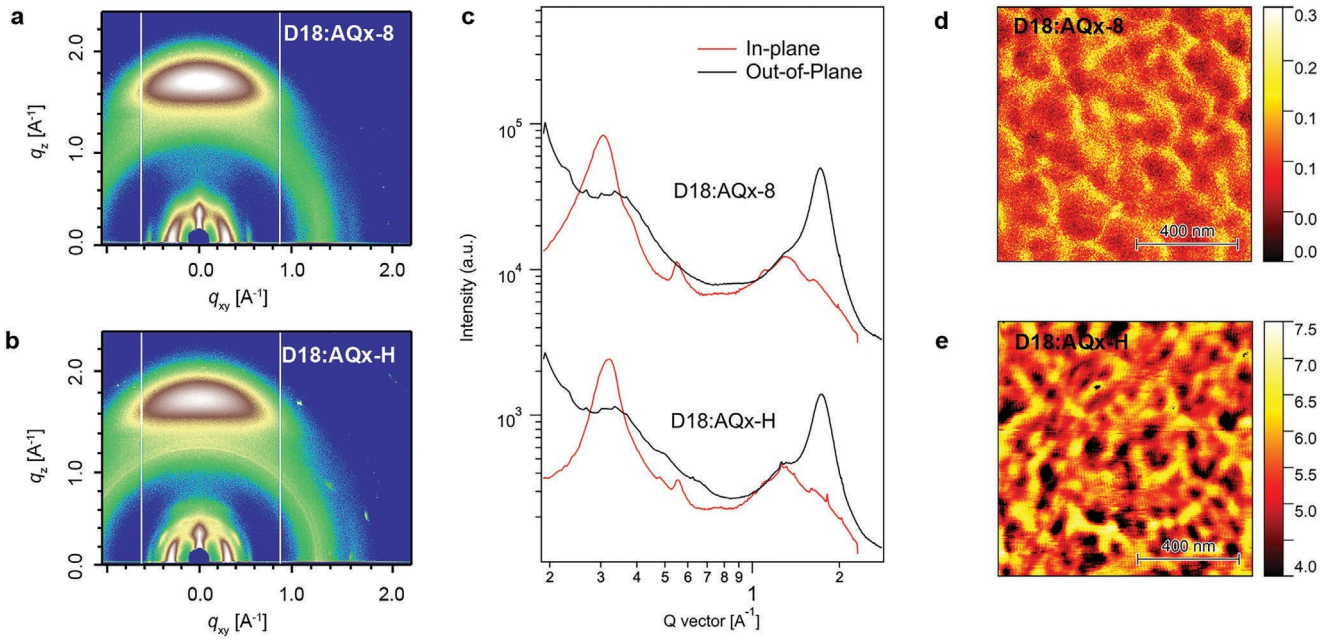

Figure 4. 2D GIWAXS patterns for a) D18:AQx-8, b) D18:AQx-H thin films. c) Line cut profiles for active layer thin films. Tapping AFM-IR image at the wavenumber of 1697 cm^{-1} for d) D18:AQx-8, e) D18:AQx-H thin films.

and IP directions in Figure 4c. Evaluation of the 2D patterns reveals that the D18:AQx-8 films exhibit enhanced lamellar and □–□ interactions, attributable to enhanced crystallinity, as evidenced by the GIWAXS analyses of the pristine films. Conversely, for the D18:AQx-H blends, the presence of some weak diffraction spots in the low-q region is discernible. The emergence of such signals insinuates a defined crystalline structure for AQx-H can be formed within the blend. Subsequent fitting of the 1D curves facilitated a quantitative appraisal of intricate crystalline parame- ters, encompassing relative crystallinity, crystal coherence length (CCL), and the paracrystalline disorder factor (g), which are col- lectively summarized in Tables S2 and S3 (Supporting Informa- tion). Relative to D18:AQx-8, the D18:AQx-H blend is character- ized by a diminished peak area for both lamellar and □-□ stack- ing peaks, indicative of the lower crystallinity of AQx-H. Nevertheless, the D18:AQx-H blend is distinguished by an augmented CCL and a diminished g-factor in comparison to D18:AQx-8. It is imperative to acknowledge that the g-factor serves as a met- ric for estimating the paracrystalline disorder for thin films, and a reduced g-factor signifies enhanced crystal quality. This phenomenon intimates that the introduction of steric hindrance at the external substitution site precipitates a reduction in the crystallinity of AQx-H within the blend. However, the crystal quality is substantially improved, exhibiting larger CCL and reduced paracrystalline disorder, suggesting a suppressed recombination. The variable temperature UV visible absorption spectrum has been supplemented in Figure S8 (Supporting Information). It is evident that during the cooling process from 100 degrees to 30 degrees, AQx-8 blue shifted by 4 nm, while AQx-H blue shifted by 6 nm, indicating stronger aggregation of AQx-H molecules.

The morphology of the blended thin films was further investigated by atomic force microscopy (AFM) and transmission electron microscopy (Figure S9, Supporting Information). The D18:AQx-8 blend film shows an inconspicuous crystal morphology and phase separation. A stronger fibrillar-type morphology is seen for D18:AQx-H blends, suggesting its good crystal habit. The atomic force microscopy-based infrared spectroscopy (AFM- IR) measurement was used to investigate the key feature of accep- tor phase in blend film by tracking the specific Fourier transform infrared (FT-IR) spectroscopy.[39–41] The AQx-8 and AQx-H display an unique FT-IR peak at 1697 cm^{-1} as shown in Figure S10 (Supporting Information), which could be used as characteristic signal to highlight the acceptor phase in the blend films. Thus, the acceptor morphology features of D18:AQx-8 and D18:AQx- H blend films could be comparatively visualized. As illustrated in Figure 4a, the thin film blend of D18:AQx-8 exhibits a fibril- lar structure on the shallow surface. Nonetheless, the signal intensity is low, rendering it challenging to discern from the background noise. This observation suggests a diminished phase pu- rity for the D18:AQx-8 blend. In contrast, the D18:AQx-H blend showcases a markedly superior fibrillar structure of AQx-H, characterized by high intensity and robust connectivity, which is required to support the charge transport. Characteristic param- eters were extracted from the AFM-IR phase images utilizing Diameter J, a software tool designed for the precise quantifi- cation of nanoscale features, as illustrated in Figures S11 and S12 (Supporting Information). The dimensions, including the length, width, and density of the fibrils, were determined and are presented in Table S4 (Supporting Information). It was observed that the D18:AQx-H blend exhibits an average fibril segmental length of 39.8 nm and a fibril density of 82.54, both values signifi- cantly exceeding those of the D18:AQx-8 blend (25.6 nm in length and 40.76 in density). This disparity indicates a better-defined network structure for AQx-H within the blend, which is advanta- geous for charge transport. Moreover, it is noteworthy that in the D18:AQx-8 blend, the mean fibril width stands at 6 nm, with the

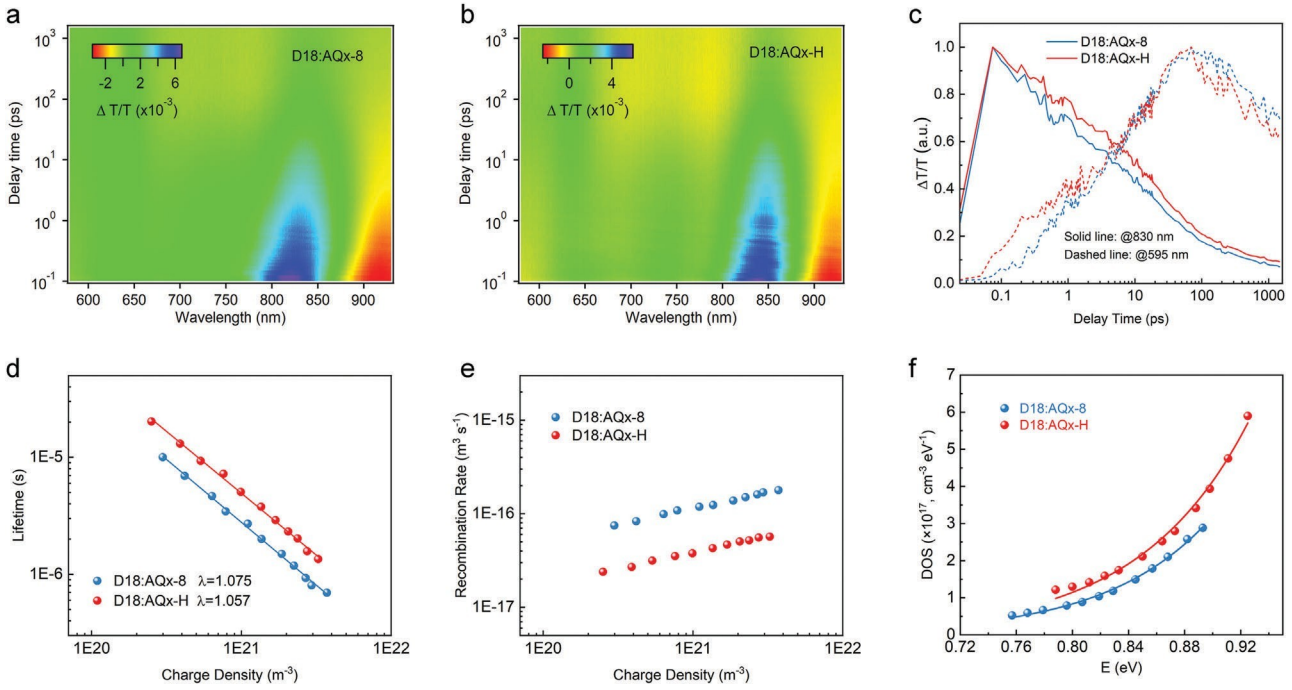

Figure 5. Color plot of TAS for a) D18:AQx-8 and b) D18:AQx-H blended film. c) Hole transfer process kinetics in corresponding conditions. Blue represents D18:AQx-8, red represents D18:AQx-H. d) Derived charge lifetime as a function of charge density fitted from TPV and TPC results. e) Recom- bination rate coefficient as a function of charge density fitted from TPV and TPC results. f) Derived LUMO DOS from the capacitance spectra of devices and detailed parameters.

maximum width reaching merely 25 nm. In stark contrast, the D18:AQx-H blend not only exhibits a mean fibril width of 10 nm but also features fibrils with widths extending beyond 60 nm, including large volume ratio of fibrils within the 20–50 nm range. This observation underscores the emergence of a multi-length-scale morphology in the D18:AQx-H blend, which likely facilitates both exciton dissociation and charge transport. The contact angle test is executed to calculated surface energy as shown in Figure S13 (Supporting Information), and the detailed parameters are summarized in Table S5 (Supporting Information). The D18, AQx-8 and AQx-H shows a surface energy of 20.71, 24.38, 27.13 mN m^{-1}, respectively. The AQx-H obtained a higher surface energy, facilitating following layer deposition. In addition, the $\gamma_{D\text{-}A}$ is calculated as 0.15 and 0.433 mN m^{-1} for D18/AQx-8 and D18/AQx-H. Higher $\gamma_{D\text{-}A}$ for D18/AQx-H exactly proved its the good crystallization property.

We further investigated the photoelectric conversion mechanism in the D18:AQx-8 and D18:AQx-H blends. The spectral and temporal characteristics of the charge-transfer dynamics in blended thin films are studied using the transient absorption spectroscopy (TAS).[42,43] The UV–vis absorption spectra of the pure D18, AQx-8, and AQx-H films, as depicted in Figure 2e, demonstrate that the donor's spectral response predominantly spans from 300 to 650 nm, and the acceptor's range covers 600–950 nm range. Thus, a 750 nm excitation is used to excite the acceptor only. The 2D spectra and representative TAS profiles at the indicated delay times are displayed in **Figure 5**a,b and Figures S14 and S15 (Supporting Information). The TAS profiles reveal that the decay traces at ≈850 nm correspond to the ground- state bleach (GSB) of the acceptor, whereas the decay traces near 920 nm are attributable to the excited state absorption of the acceptor. The decline of the acceptor bleach peak at 830 nm, accompanied by the rise of the donor GSB peak at ≈595 nm, signifies the hole-transfer process from the acceptor to the donor. These profiles are summarized in Figure 5c, and fitted by biexponential function to obtain the kinetics (Table S6, Supporting Information). The rapid components (τ_1) represent the kinetics of the exciton dissociation in mixing domain or at interfaces, registering at 0.48 and 0.26 ps for the AQx-8 and AQx-H blends, respectively. Conversely, the more prolonged components (τ_2) reflect the kinetics of exciton migration in crystalline domain, necessitating an additional diffusion process toward the interface. The temporal values τ_2 associated with these processes are 15.72 and 15.61 ps for the AQx-8 and AQx-H blends, respectively. The reduced τ_1 indicates that AQx-H leads to a more favourable donor-acceptor interaction in mixing region, thus hole-transfer process is expedited. Regarding τ_2, the temporal values for both the D18:AQx-8 and D18:AQx-H blends exhibit similarity. This observation suggests that, notwithstanding the greater crystal size observed along the lamellar direction in the D18:AQx-H blend, there is an enhancement in exciton diffusion capability. This improvement can be attributed to the superior crystalline quality of the D18:AQx-H blend. This phenomenon underscores the critical interrelationship between crystalline dimensions and quality with the intrinsic exciton diffusion properties, highlight- ing the nuanced mechanisms governing exciton mobility within these blended materials. The falling edge at @595 nm shown in Figure 5c could be used to evaluate the lifetime of the generated holes. The photocurrent density-effective voltage characteriza- tion was carried out with results shown in Figure S16 (Supporting

Information). The carrier collection efficiency P(E, T) values are 95.09% and 95.58% (Table S7, Supporting Information) for the D18:AQx-8 and D18:AQx-H blends, respectively, contributing to high J_{SC} for corresponding devices of D18:AQx-H despite the blue shift in the spectrum. The Hansen Solubility Parameter (HSP) was calculated by group contribution methods based on materials' chemical structure. The molecular interaction is thought to be stronger, when the solubility parameters (□) value closer. The d of D18, AQx-8 and AQx-H are 23.80, 22.93, 24.18, respectively. As shown in Figure S17 (Supporting Information), the □ of D18 is closer with AQx-H (0.38) than AQx-8 (0.87). Such a result suggests that improved donor–acceptor interaction is obtained between D18 and AQx-H, which is consistent with the TAS results. The relevant data and content have been complemented to the latest version of the manuscript.

Charge transport and recombination dynamics were elucidated through transient photovoltage (TPV) and transient photocurrent (TPC) assessments.[44] The derived charge lifetimes (τ_c) and charge density (n) under varying V_{OC} conditions are summarized in Figure S18 (Supporting Information). Both τ_c and n for D18:AQx-H devices register higher value across the applied V_{OC} region, which is ascribed to a reduced charge recombination, suggesting less defects and energetic disorder in D18:AQx-H blends. The charge lifetime as a function of charge density is graphically represented in Figure 5d, adhering to an approximately exponential law of

$$\tau_c = \tau_0 \left(\frac{1}{n_0}\right)^{\beta} \quad (2)$$

where τ_0 and n_0 are constants, while the exponential factor □ correlates with the non-geminate recombination order R, where R = □ + 1. In scenarios where bimolecular recombination predominates as the loss mechanism within the device, R tends toward 2. Conversely, when trap-assisted recombination prevails, R is anticipated to exceed 2. The D18:AQx-H device exhibits a minimum R of 2.057 with the maximum lifetimes, thereby indicating a minimization of non-geminate recombination. Similar conclusions can be drawn from light intensity dependent J_{SC} and V_{OC} measurements (Figure S19 and Table S8, Supporting Information). The non-geminate recombination rate coefficient k(n) follows the equation of

$$k(n) = \frac{1}{\tau_c(n) \times n} \quad (3)$$

where τ_c(n) is the carrier lifetime. The variation of k(n) across different charge densities is depicted in Figure 5e, demonstrating a markedly reduced recombination rate for the D18:AQx-H blended thin film over an extensive range of charge densities. This conclusion is further corroborated by the Space Charge Limited Current measurements, as documented in Table S9 and Figure S20 (Supporting Information), reinforcing the evidence of suppressed recombination within the D18:AQx-H blend.

The dark J–V curves of the optimal devices are shown in Figure S21 (Supporting Information). The D18:AQx-H device shows reduced reverse saturated current densities, indicating improved diode characteristics with a low leaking current. In the forward direction, the D18:AQx-H device shows an early transition from Ohmic to semiconductor zones and higher saturation value, indicating a higher charge density.[45] The calculated rectification ratios at ± 1.0 V are 6.5×10^1 and 7.2×10^2 for D18:AQx-8 and D18:AQx-H devices, respectively, which is in consistence with the FFs.[46] The fundamental electronic property of the blended thin films is studied by the electron density of state (DOS) characterization.[47] As shown in Figure 5f, the D18:AQx-H device demonstrates a much higher density of states, which extends the V_{OC} to over 0.92 V. These findings are in concordance with the outcomes derived from preceding optical and physical evaluations, corroborating the premise that an augmented charge density and enhanced charge transfer significantly contribute to the elevated J_{SC} and FF in D18:AQx-H devices.

The simulation of the optical electric field $|E(x)^2|$ distribution, conducted using the transfer matrix method, was employed to access the photoelectric properties within the device layers.[48] The optical constants, including the refractive-index (n) and extinction-coefficient (k) for the blends and all ancillary layers, are defined and depicted in Figure S22 (Supporting Information). The detailed parameters are summarized in Table S10 (Supporting Information). The 2D color filled contour plot of the optical electric field $|E(x)|^2$ within the devices of D18:AQx-H and the D18:AQx-H device with optimized thickness for each layer are presented in Figure S23 (Supporting Information). Notably, the intensity of $|E(x)|^2$ in D18:AQx-H blend is enhanced and exhibits a shifts toward the short-wavelength direction compared with the D18:AQx-8 blend device beyond 750 nm. This observation is in alignment with the UV–vis absorption spectrum shown in Figure 2e and TA results in Figure S15 (Supporting Information). Figure S24 (Supporting Information) delineates the energy distribution Q of D18:AQx-8 and D18:AQx-H with optimized photoactive layer thickness. A significant improvement in intensity within the 670–820 nm range is observed in the D18:AQx-H blends, conforming to the conclusions of P(E, T) values in Figure S16 (Supporting Information) and EQE measurement in Figure 3d. These findings elucidate the advantages of the D18:AQx-H device in this optimal thickness.

In summary, a new NFA material AQx-H was designed and synthesized, which features with shorter length and high steric hindrance cyclohexane side chain. Compared to linear side chain analogue (AQx-8), AQx-H shows blue-shifted photon absorption. However, its enhanced molar absorption coefficient and efficient photon-to-electron conversion afford a comparable J_{SC}. In addition, the raised LUMO energy level improves its V_{OC}. Morphology studies show that the introduction of cyclohexane substituents reduces the crystallinity of the NFA but enhances phase separation. As a result, much better multi-length scale fibril-like morphology with better crystal quality is observed in D18:AQx-H blends, promoting more efficient exciton dissociation and charge transport. The AQx-based OSC exhibited a PCE of 19.5% with a high V_{OC} of 0.923 V, J_{SC} of 26.40 mA cm^{-2}, and FF of 79.87%, which much higher than that of AQx-8-based binary device (17.8%). These results demonstrate that appropriate design of the alkyl side chain, as seen here of using cyclohexane with enhanced steric hindrance and reduced inter-mixing between donor/acceptor materials is a promising strategy for designing high V_{OC} NFAs to achieve high PCEs.

3. Experimental Section

See experimental details in the Supporting information.

Supporting Information

Supporting Information is available from the Wiley Online Library or from the author.

Acknowledgements

This work was financially supported by the National Natural Science Foundation of China (Grant No. 22171273, 52325306, 22379094, and 22309111), the Science and Technology Commission of Shanghai Munic- ipality (Grant No. 21DZ1208602) and the Center of Hydrogen Science, Shanghai Jiao Tong University, China. S.X. acknowledges the support from the Shanghai Rising-Star Program (23QA1405100). M.Z. acknowledges the funding supported by the Postdoctoral Innovative Talent Support Pro- gram (Grant No. BX20220203) and the China Postdoctoral Science Foun- dation (Grant No. 2022M722072). The synchrotron x-ray scattering tests were carried out at beamline 7.3.3 at the Advanced Light Source, Lawrence Berkeley National Laboratory, supported by the DOE, Office of Science, and Office of Basic Energy Sciences.

Conflict of Interest

The authors declare no conflict of interest.

Data Availability Statement

The data that support the findings of this study are available from the cor- responding author upon reasonable request.

Keywords

cyclohexane, non-fullerene acceptors, open-circuit voltage, organic solar cells, quinoxaline

Received: April 7, 2024
Revised: May 13, 2024
Published online:

[1] Y. Li, X. Huang, H. K. M. Sheriff, S. R. Forrest, *Nat. Rev. Mater.* **2023**, *8*, 186.
[2] G. Yu, J. Gao, J. C. Hummelen, F. Wudl, A. J. Heeger, *Science* **1995**, *270*, 1789.
[3] G. Li, R. Zhu, Y. Yang, *Nat. Photonics* **2012**, *6*, 153.
[4] L. Lu, T. Zheng, Q. Wu, A. M. Schneider, D. Zhao, L. Yu, *Chem. Rev.* **2015**, *115*, 12666.
[5] H. Kang, G. Kim, J. Kim, S. Kwon, H. Kim, K. Lee, *Adv. Mater.* **2016**, *28*, 7821.
[6] H. Lu, W. Liu, G. Ran, Z. Liang, H. Li, N. Wei, H. Wu, Z. Ma, Y. Liu, W. Zhang, X. Xu, Z. Bo, *Angew. Chem., Int. Ed.* **2023**, *135*, e202314420.
[7] M. Zhang, X. Guo, W. Ma, H. Ade, J. Hou, *Adv. Mater.* **2015**, *27*, 4655.
[8] Y. Lin, J. Wang, Z.-G. Zhang, H. Bai, Y. Li, D. Zhu, X. Zhan, *Adv. Mater.* **2015**, *27*, 1170.
[9] J. Yuan, Y. Zhang, L. Zhou, G. Zhang, H.-L. Yip, T.-K. Lau, X. Lu, C. Zhu, H. Peng, P. A. Johnson, M. Leclerc, Y. Cao, J. Ulanski, Y. Li, Y. Zou, *Joule* **2019**, *3*, 1140.
[10] Q. Liu, Y. Jiang, K. Jin, J. Qin, J. Xu, W. Li, J. Xiong, J. Liu, Z. Xiao, K. Sun, S. Yang, X. Zhang, L. Ding, *Sci. Bull.* **2020**, *65*, 272.
[11] W. Wei, C. Zhang, Z. Chen, W. Chen, G. Ran, G. Pan, W. Zhang, P. Buschbaum, Z. Bo, C. Yang, Z. Luo, *Angew. Chem., Int. Ed.* **2024**, *63*, e202315625.
[12] S. Xu, Z. Zhou, W. Liu, Z. Zhang, F. Liu, H. Yan, X. Zhu, *Adv. Mater.* **2017**, *29*, 1704510.
[13] L. Meng, Y. Zhang, X. Wan, C. Li, X. Zhang, Y. Wang, X. Ke, Z. Xiao, L. Ding, R. Xia, H.-L. Yip, Y. Cao, Y. Chen, *Science* **2018**, *361*, 1094.
[14] Y. Ma, M. Zhang, S. Wan, P. Yin, P. Wang, D. Cai, F. Liu, Q. Zheng, *Joule* **2021**, *5*, 197.
[15] X. Wang, H. Lu, Y. Liu, A. Zhang, N. Yu, H. Wang, S. Li, Y. Zhou, X. Xu, Z. Tang, Z. Bo, *Adv. Energy Mater.* **2021**, *11*, 2102591.
[16] L. Zhu, M. Zhang, J. Xu, C. Li, J. Yan, G. Zhou, W. Zhong, T. Hao, J. Song, X. Xue, Z. Zhou, R. Zeng, H. Zhu, C.-C. Chen, R. C. I. MacKenzie, Y. Zou, J. Nelson, Y. Zhang, Y. Sun, F. Liu, *Nat. Mater.* **2022**, *21*, 656.
[17] Z. Jia, Q. Ma, Z. Chen, L. Meng, N. Jain, I. Angunawela, S. Qin, X. Kong, X. Li, Y. M. Yang, H. Zhu, H. Ade, F. Gao, Y. Li, *Nat. Commun.* **2023**, *14*, 1236.
[18] M. Zhang, L. Zhu, T. Hao, G. Zhou, C. Qiu, Z. Zhao, N. Hartmann, B. Xiao, Y. Zou, W. Feng, H. Zhu, M. Zhang, Y. Zhang, Y. Li, T. Russell, F. Liu, *Adv. Mater.* **2021**, *33*, 2007177.
[19] H. Liang, X. Bi, H. Chen, T. He, Y. Lin, Y. Zhang, K. Ma, W. Feng, Z. Ma, G. Long, C. Li, B. Kan, H. Zhang, O. A. Rakitin, X. Wan, Z. Yao, Y. Chen, *Nat. Commun.* **2023**, *14*, 4707.
[20] H. Hu, S. Liu, J. Xu, R. Ma, Z. Peng, T. A. D. Peña, Y. Cui, W. Liang, X. Zhou, S. Luo, H. Yu, M. Li, J. Wu, S. Chen, G. Li, Y. Chen, *Angew. Chem., Int. Ed.* **2023**, *62*, e202400086.
[21] Y. A. Shi, Y. L. Chang, K. Lu, Z. H. Chen, J. Q. Zhang, Y. J. Yan, D. D. Qiu, Y. A. Liu, M. A. Adil, W. Ma, X. T. Hao, L. Y. Zhu, Z. X. Wei, *Nat. Commun.* **2022**, *13*, 3256.
[22] C. Li, J. Zhou, J. Song, J. Q. Xu, H. Zhang, X. Zhang, J. Guo, L. Zhu, D. Wei, G. Han, J. Min, Y. Zhang, Z. Xie, Y. Yi, H. Yan, F. Gao, F. Liu, Y. Sun, *Nat. Energy* **2021**, *6*, 605.
[23] M. Zhang, L. Zhu, G. Zhou, T. Hao, C. Qiu, Z. Zhao, Q. Hu, B. Larson, H. Zhu, Z. Ma, Z. Tang, W. Feng, Y. Zhang, T. Russell, F. Liu, *Nat. Commun.* **2021**, *12*, 309.
[24] Y. Liang, D. Zhang, Z. Wu, T. Jia, L. Lüer, H. Tang, L. Hong, J. Zhang, K. Zhang, C. J. Brabec, N. Li, F. Huang, *Nat. Energy* **2022**, *7*, 1180.
[25] W. Song, Q. Ye, S. Yang, L. Xie, Y. Meng, Z. Chen, Q. Gu, D. Yang, J. Shi, Z. Ge, *Angew. Chem., Int. Ed.* **2023**, *62*, e202310034.
[26] F. Liu, Y. Jiang, R. Xu, W. Su, S. Wang, Y. Zhang, K. Liu, S. Xu, W. Zhang, Y. Yi, W. Ma, X. Zhu, *Angew. Chem., Int. Ed.* **2024**, *63*, e202313791.
[27] K. Jiang, J. Zhang, C. Zhong, F. R. Lin, F. Qi, Q. Li, Z. Peng, W. Kaminsky, S.-H. Jang, J. Yu, X. Deng, H. Hu, D. Shen, F. Gao, H. Ade, M. Xiao, C. Zhang, A. K. Y. Jen, *Nat. Energy* **2022**, *7*, 1076.
[28] Q. Fan, R. Ma, J. Yang, J. Gao, H. Bai, W. Su, Z. Liang, Y. Wu, L. Tang, Y. Li, Q. Wu, K. Wang, L. Yan, R. Zhang, F. Gao, G. Li, W. Ma, *Angew. Chem., Int. Ed.* **2023**, *62*, e202308307.
[29] R. Sun, Y. Wu, X. Yang, Y. Gao, Z. Chen, K. Li, J. Qiao, T. Wang, J. Guo, C. Liu, X. Hao, H. Zhu, J. Min, *Adv. Mater.* **2022**, *34*, 2110147.
[30] L. Hong, H. Yao, Z. Wu, Y. Cui, T. Zhang, Y. Xu, R. Yu, Q. Liao, B. Gao, K. Xian, H. Y. Woo, Z. Ge, J. Hou, *Adv. Mater.* **2019**, *31*,

1903441.
[31] K. Jiang, Q. Wei, J. Y. L. Lai, Z. Peng, H. K. Kim, J. Yuan, L. Ye, H. Ade, Y. Zou, H. Yan, *Joule* **2019**, *3*, 3020.
[32] G. Chai, Y. Chang, J. Zhang, X. Xu, L. Yu, X. Zou, X. Li, Y. Chen, S. Luo, B. Liu, F. Bai, Z. Luo, H. Yu, J. Liang, T. Liu, K. S. Wong, H. Zhou, Q. Peng, H. Yan, *Energy Environ. Sci.* **2021**, *14*, 3469.
[33] W. Liu, J. Zhang, S. Xu, X. Zhu, *Sci. Bull.* **2019**, *64*, 1144.
[34] Z. Zhou, W. Liu, G. Zhou, M. Zhang, D. Qian, J. Zhang, S. Chen, S. Xu, C. Yang, F. Gao, H. Zhu, F. Liu, X. Zhu, *Adv. Mater.* **2020**, *32*, 1906324.
[35] Y. Jiang, Y. Li, F. Liu, W. Wang, W. Su, W. Liu, S. Liu, W. Zhang, J. Hou, S. Xu, Y. Yi, X. Zhu, *Nat. Commun.* **2023**, *14*, 5079.
[36] D. Qian, Z. Zheng, H. Yao, W. Tress, T. R. Hopper, S. Chen, S. Li, J. Liu, S. Chen, J. Zhang, X.-K. Liu, B. Gao, L. Ouyang, Y. Jin, G. Pozina, I. A. Buyanova, W. M. Chen, O. Inganäs, V. Coropceanu, J.-L. Bredas, H. Yan, J. Hou, F. Zhang, A. A. Bakulin, F. Gao, *Nat. Mater.* **2018**, *17*, 703.
[37] R. Yu, R. Shi, H. Liu, G. Wu, Z. Ma, H. Gao, Z. He, Z. Tan, *Adv. Energy Mater.* **2022**, *12*, 2201306.
[38] J. Song, M. Zhang, M. Yuan, Y. Qian, Y. Sun, F. Liu, *Small Methods* **2018**, *2*, 1700229.
[39] F. Li, T. W. Lo, X. Deng, S. Li, Y. Fan, F. R. Lin, Y. Cheng, Z. Zhu, D. Lei, A. K. Y. Jen, *Adv. Energy Mater.* **2022**, *12*, 2200186.
[40] Y. Zhao, P. Zhu, M. Wang, S. Huang, Z. Zhao, S. Tan, T. H. Han, J. W. Lee, T. Huang, R. Wang, J. Xue, D. Meng, Y. Huang, J. Marian, J. Zhu, Y. Yang, *Adv. Mater.* **2020**, *32*, 1907769.
[41] R. Wang, J. Xue, L. Meng, J.-W. Lee, Z. Zhao, P. Sun, L. Cai, T. Huang, Z. Wang, Z.-K. Wang, Y. Duan, J. L. Yang, S. Tan, Y. Yuan, Y. Huang, Y. Yang, *Joule* **2019**, *3*, 1464.
[42] G. Zhou, M. Zhang, Z. Chen, J. Zhang, L. Zhan, S. Li, L. Zhu, Z. Wang, X. Zhu, H. Chen, L. Wang, F. Liu, H. Zhu, *ACS Energy Lett.* **2021**, *6*, 2971.
[43] G. Zhou, M. Zhang, J. Xu, Y. Yang, T. Hao, L. Zhu, L. Zhou, H. Zhu, Y. Zou, G. Wei, Y. Zhang, F. Liu, *Energy Environ. Sci.* **2022**, *15*, 3483.
[44] R. Hamilton, C. G. Shuttle, B. O'Regan, T. C. Hammant, J. Nelson, J. R. Durrant, *J. Phys. Chem. Lett.* **2010**, *1*, 1432.
[45] M. C. Schlamp, X. G. Peng, A. P. Alivisatos, *J. Appl. Phys.* **1997**, *82*, 5837.
[46] R. Zeng, L. Zhu, M. Zhang, W. Zhong, G. Zhou, J. Zhuang, T. Hao, Z. Zhou, L. Zhou, N. Hartmann, X. Xue, H. Jing, F. Han, Y. Bai, H. Wu, Z. Tang, Y. Zou, H. Zhu, C. Chen, Y. Zhang, F. Liu, *Nat. Commun.* **2023**, *14*, 4148.
[47] J. C. Blakesley, D. Neher, *Phys. Rev.B* **2011**, *84*, 075210.
[48] R. Yu, R. Shi, Z. He, T. Zhang, S. Li, Q. Lv, S. Sha, C. Yang, J. Hou, Z. Tan, *Chem. Int. Ed.* **2023**, *62*, e202308367.